J. Fluid Mech. (2001), *vol.* 443, *pp.* 101–128. Printed in the United Kingdom

© 2001 Cambridge University Press

Shear-induced particle diffusivities from numerical simulations

By MARCO MARCHIORO† AND ANDREAS ACRIVOS

The Levich Institute, T-1M, The City College of the City University of New York, New York, NY 10031, USA

(Received 25 May 2000 and in revised form 15 March 2001)

Using Stokesian dynamics simulations, we examine the flow of a monodisperse, neutrally buoyant, homogeneous suspension of non-Brownian solid spheres in simple shear, starting from a large number of independent hard-sphere distributions and ensemble averaging the results. We construct a novel method for computing the gradient diffusivity via simulations on a *homogeneous* suspension and, although our results are only approximate due to the small number of particles used in the simulations, we present here the first values of this important parameter, both along and normal to the plane of shear, to be obtained directly either experimentally or numerically. We show furthermore that, although the system of equations describing the particle motions is deterministic, the particle displacements in the two directions normal to the bulk flow have Gaussian distributions with zero mean and a variance which eventually grows linearly in time thereby establishing that the system of particles is diffusive. For particle concentrations up to 45%, we compute the corresponding tracer diffusivities both from the slope of the mean-square particle displacement and by integrating the corresponding velocity autocorrelations and find good agreement between the two sets of results.

1. Introduction

It is generally accepted now that shear-induced particle diffusion in a shear flow, under conditions of vanishingly small Reynolds numbers, plays a key role in the dynamic behaviour of concentrated suspensions of non-Brownian particles (see Acrivos 1995). This phenomenon has been studied extensively, both experimentally as well as computationally (Breedveld *et al.* 1998; Bossis & Brady 1987), and several models have been proposed and then tested experimentally for determining the particle concentration profiles and flow characteristic of such suspensions under a variety of conditions (Leighton & Acrivos 1987*b*; Phillips *et al.* 1992; Nott & Brady 1994). Here we consider a monodisperse suspension of neutrally buoyant spheres in a simple shear flow and, by means of computer simulations, focus on the three basics aspects of this rapidly evolving field: (i) the statistics of the particle displacements; (ii) the evaluation of the particle tracer diffusivity via both the evolution with time of the mean-square particle displacement as well as from the integral of the velocity autocorrelation function; (iii) the determination of the gradient diffusivity from the particle trajectories in a *homogeneous* suspension.

The aim of the first part of the paper is to consider further the question, which has been raised in the past by several investigators in this field, as to whether diffusion

† Present address: RiskMap SpA, via Gian Battista Vico 4, Milan, Italy.

https://doi.org/10.1017/S0022112001005122 Published online by Cambridge University Press

can possibly arise from a deterministic time evolution of the configuration of the system of particles in a space-filling suspension undergoing shear. To resolve this issue, we shall present the results of numerical simulations which show that, under a variety of conditions, a tracer particle diffuses in a homogeneous suspension being sheared even under the action of exclusively deterministic forces. In this context, a system is said to be diffusive if any of its coordinates has a displacement which, at least for large times, has a Gaussian distribution with zero mean, and a variance that grows linearly with time. We shall also show that our simulations give rise to a macroscopic irreversibility even though the system being modelled is reversible on a microscale.

The second part of the paper concerns the particle tracer diffusivity. Traditionally, see Bossis & Brady (1987), this coefficient has been obtained starting from a single hard-sphere particle configuration and then computing particle displacements over time intervals which, even for a monolayer, were typically at least two orders of magnitude larger than $1/\gamma$, the characteristic time of the applied shear rate γ. Here, guided by the recent experiments of Breedveld *et al.* (1998) who evaluated the tracer diffusivity using a large amount of independent displacement data taken over time intervals $1/\gamma$ or even lower, we performed simulations starting from a large number of independent hard-sphere particle configurations and, after shearing the suspension for times $5/\gamma$ to $10/\gamma$, depending on the particle concentration, in order to achieve the equilibrium particle configurations pertaining to a homogeneous suspension in a simple shear, computed the diffusivity along and normal to the plane of shear from the ensemble average of the square displacement of the particles, as well as, apparently for the first time from numerical simulations, from the integral of the corresponding velocity autocorrelation function. Close agreement was found between the values of the tracer diffusivity using the two methods just mentioned.

In the third part of this paper we present the first computed values of the gradient diffusivities, again along and normal to the plane of shear, which were obtained by applying a technique recently developed by Marchioro, Tanksley & Prosperetti (2000, 2001), for the purpose of constraining closure relations in suspensions. The great advantage of this technique is that all the computations are performed on a *homogeneous* suspension. The values for the gradient diffusivity thus computed are in good agreement with the small amount of available experimental data, considering the small number of spheres used in our simulations.

2. Simulation method

The calculation of the diffusion coefficients is based on the numerical simulation of a suspension of spheres in a simple shear flow under Stokes flow conditions, and in the absence of Brownian and buoyancy effects. Although, in principle, any simulation method would do, we have chosen to use the well-known method of Stokesian dynamics of Brady & Bossis (1988) which has been developed specifically for computing the hydrodynamic interactions among an infinite suspension of particles at zero Reynolds numbers.

As already shown by Brady & Bossis (1985), in concentrated suspensions, adjacent spheres interacting purely through hydrodynamic forces spend a great deal of time almost in contact with one another with the corresponding separation distances being less than 10^{-8} sphere radii. Also Dratler & Schowalter (1996) (see also Melrose & Ball 1995) found that, if the non-overlapping condition was strictly enforced, this minimum separation distance depended on the time step of integration, in the sense

https://doi.org/10.1017/S0022112001005122 Published online by Cambridge University Press

that adjacent spheres came closer and closer together as this time step was decreased. All the authors referred to above also concluded, however, that such simulations could still be performed provided a small repulsive force was introduced between adjacent pairs of particles in very close proximity to each other. The simulation results were then found to be independent of the detailed expression of this force provided it was sufficiently short ranged. The introduction of such a force actually models, at least qualitatively, the behaviour of real physical systems in that, in the gaps between the particles, the presence of residual Brownian forces and/or the roughness of the spheres always play a central role.

For this inter-particle force we used the expression for the repulsive force between two spheres, already well-tested in Stokesian dynamics simulations (Brady & Bossis 1985),

$$\boldsymbol{F}_{\alpha\beta} = F_0 \frac{\lambda \mathrm{e}^{-\lambda\varepsilon}}{1 - \mathrm{e}^{-\lambda\varepsilon}} \boldsymbol{e}_{\alpha\beta}\,, \tag{2.1}$$

where $6\pi\mu a^2\gamma \boldsymbol{F}_{\alpha\beta}$, with μ being the viscosity of the suspending liquid and a the sphere radius, is the force exerted on sphere α by sphere β, F_0 is a dimensionless coefficient reflecting the magnitude of this force, λ is related to the range of the force, ε is the distance of closest approach between the surfaces of the two spheres divided by a, and $\boldsymbol{e}_{\alpha\beta}$ is the unit vector connecting their centres pointing from β to α. In the simulations reported here, λF_0 was chosen to be unity and $\lambda = 1000$. Simulations using other values for these parameters, namely $\lambda = 10^4, 10^5, 10^6$ and $F_0 = 1, 10^{-1}, 10^{-2}$, gave similar results.

The detailed description of the simulation method can be found elsewhere, see e.g. Brady & Bossis (1988), hence we provide here only a brief overview. We consider the zero Reynolds number flow of a suspension of hard spheres in simple shear characterized by a shear rate γ. The spheres are placed in a periodic box, typically a cube with dimensions uniquely determined by the number of spheres N and the volume fraction ϕ, and periodic boundary conditions are applied. The volume of the box V, the number of spheres N and the volume fractions ϕ are related by the expression

$$\phi = \frac{4\pi N a^3}{3V}\,. \tag{2.2}$$

Let x, y, and z be, respectively, the directions of the imposed shear flow, the velocity gradient, and the vorticity, and let v and w be the components of the particle velocity in the y- and z-directions, respectively. If $\boldsymbol{x}_N$ denotes the $3N$-dimensional vector of the position of the particles, the evolution of the particle trajectory can be represented by

$$\delta \boldsymbol{x}_N = \delta \boldsymbol{x}^a + \delta \boldsymbol{x}^H + \delta \boldsymbol{x}^F\,, \tag{2.3}$$

where $\delta \boldsymbol{x}^a$ is the affine displacement in the x-direction due to the imposed shear, $\delta \boldsymbol{x}^H$ is the displacement due to pure hydrodynamic interactions, and $\delta \boldsymbol{x}^F$ is the displacement due to the inter-particle force defined in (2.1). A large number N_c, typically a few hundred, of simulations were performed starting from different initial hard-sphere configurations.

The computational cost of calculating both the many-body far-field interactions and the pairwise-additive lubrication forces between the particles is $O(N^3)$ for a single configuration, where N is the number of spheres in the unit cell. In our case, this limited the number of particles in the unit cell to be not greater than 64.

In what follows, all the variables have been rendered dimensionless using the radius

https://doi.org/10.1017/S0022112001005122 Published online by Cambridge University Press

of the spheres a as the characteristic length scale and γ^{-1}, the inverse of the imposed strain rate, as the characteristic time. As a consequence the diffusivities are scaled by $a^2\gamma$.

3. Statistics of the particle displacement

There exists experimental evidence that, even at vanishingly small Reynolds numbers and seemingly negligible Brownian force effects, particles in a concentrated suspension exhibit diffusive behaviour (Leighton & Acrivos 1987*a*). More recently, it was also shown by Breedveld *et al.* (1998) that, in a sheared suspension at effectively infinite Péclet numbers, the displacements of tagged particles have an approximately Gaussian distribution even when evaluated for small time intervals.

In a physical experiment, however, particles are not perfectly spherical and a residual Brownian motion as well as minute inertia effects are always present within the suspension, hence it appears reasonable to suppose that non-deterministic irreversible forces cannot be completely eliminated under even the most idealized experimental conditions. The advantage of numerical simulations, on the other hand, is that it is possible to control more precisely all the parameters that affect the flow and, at least in principle, eliminate completely all non-deterministic and irreversible forces.

The first goal of the present paper is to show, from Stokesian dynamics simulations, that particle diffusion in a sheared suspension can take place even under the action of exclusively deterministic forces. This should not come as a surprise given that, as is well known, even low-dimensional deterministic dynamical systems can exhibit diffusion (see Schuster 1989, p. 32) which is usually taken as a sign of chaotic behaviour. Although we have not been able to prove that the system of equations describing the evolution of the particle positions is chaotic, we suggest that this is a reasonable hypothesis and indeed the cause of the phenomenon of shear-induced diffusion. To this end we shall first examine the statistical properties of the displacement of a test particle in a sheared suspension.

Consider then N spherical particles in the unit box flowing under shear. Denoting by $y(\tau)$ the y-coordinate of a generic particle at time τ, we focus on the statistics of

$$\Delta y = y(\tau + t) - y(\tau), \tag{3.1}$$

where τ is taken to be large enough to ensure that there is no dependence on the initial hard-spheres particle distribution (in our simulations $\tau \simeq 5$ is sufficient). The determination of the statistical properties of Δy, i.e. its p.d.f., requires a large number of samples.

Since the Stokesian dynamics code did not allow us to simulate systems with more than about 100 particles, we relied on data for Δy as obtained from a large number N_c of different simulations starting with N_c independent hard-sphere configurations. In this way the number of samples available for the determination of the statistics of Δy was enlarged to $N \times N_c$ (since the computational cost is $O(N^3 N_c)$, it is convenient to choose N small and N_c large). Alternatively, a large number of different Δy could have been taken from different time slices of a single configuration running for a long time. We checked that both approaches give the same p.d.f.

Figure 1 shows the p.d.f. of (*a*) Δy and (*b*) Δz as obtained with $N = 16$ and $N_c = 512$ at a volume fraction $\phi = 0.25$, for different t and for $\tau = 5$, together with the plot of the Gaussian distributions with the same variance as the numerical data. It is evident to the eye that the distributions of both Δy and Δz are approximately Gaussian and, indeed, the calculations of higher moments confirm that the Gaussian distribution

https://doi.org/10.1017/S0022112001005122 Published online by Cambridge University Press

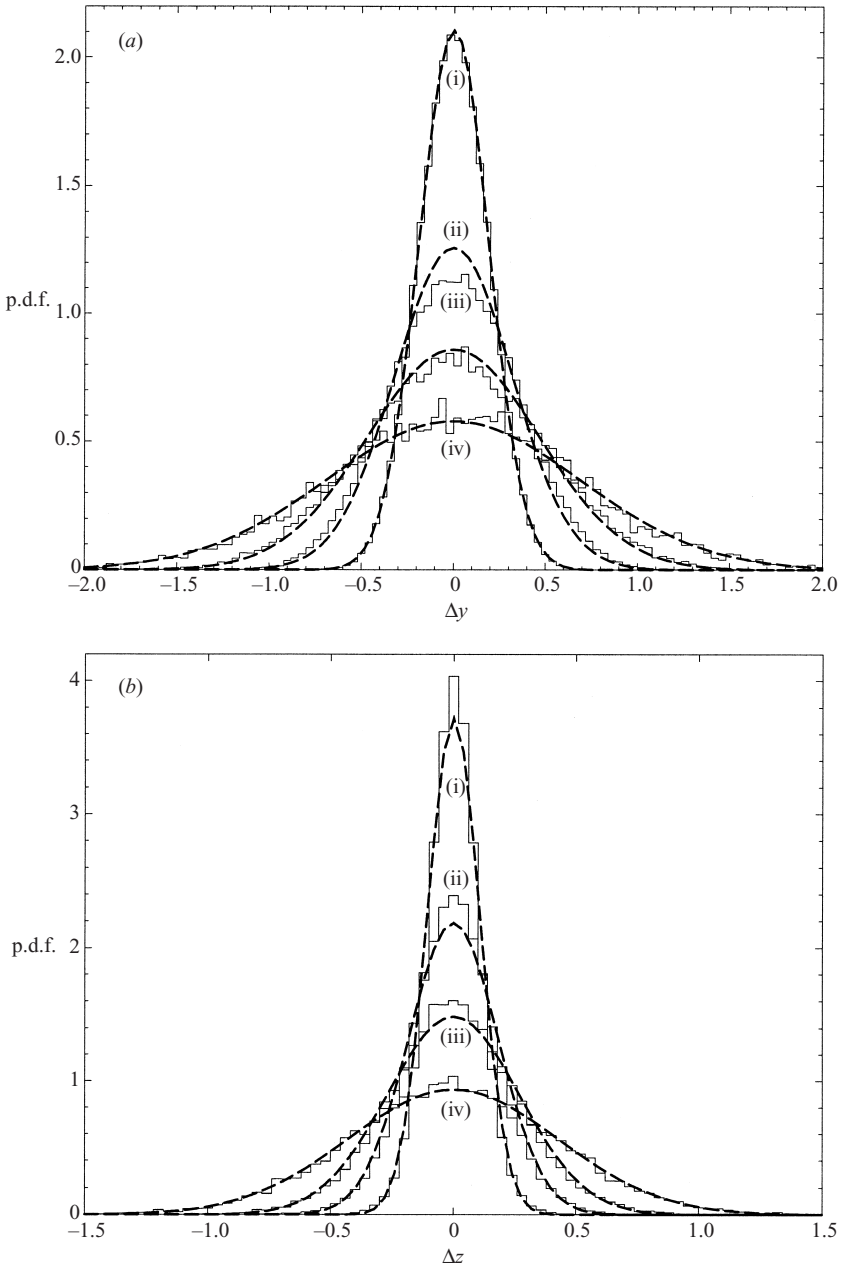


FIGURE 1. The probability density function (p.d.f.) of (*a*) Δy and (b) Δz, thin solid line, for $\tau = 5$, $N = 16$, $N_c = 512$, and $\phi = 0.25$; (i) $t = 0.5$, (ii) $t = 1$, (iii) $t = 2$, and (iv) $t = 8$. The dashed lines are the density functions for a Gaussian distribution with zero mean and the same variance as the numerical data.

is approached for increasing t. A similar distribution for the displacements of the particle positions was observed experimentally by Breedveld *et al.* (1998).

The fact that the displacements have a Gaussian distribution suggests that some randomness entered the system, but does not mean as yet that the particles actually diffuse. To prove diffusion, it is necessary to show that the variance of the particle

https://doi.org/10.1017/S0022112001005122 Published online by Cambridge University Press

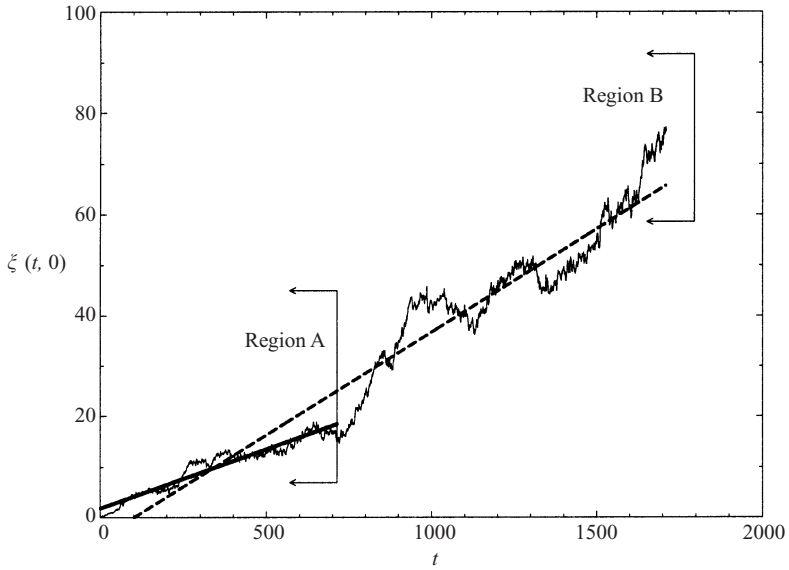


FIGURE 2. Plot of $\xi(t,\tau)$, as defined in (3.2), for $\tau = 0$, $N = 27$, $\phi = 0.35$. The two straight lines are linear least-squares fits in region A (thick solid line) and region B (dashed line).

displacements grows linearly in time. To this end let us define

$$\xi(t,\tau) = \frac{1}{2N}\sum_{\alpha=1}^{N}[y^{\alpha}(\tau+t) - y^{\alpha}(\tau)]^2, \quad \tau \geqslant 0, \tag{3.2}$$

where $y^{\alpha}(t+\tau)$ is the y-coordinate of particle α at time $t+\tau$ starting from a single initial hard-sphere distribution. If diffusion is indeed present in such a system, then ξ should eventually grow linearly with t with the diffusion coefficient being equal to the slope of this curve. Figure 2 shows a plot of $\xi(t,0)$ for $N = 27$, $\phi = 0.35$, up to $t = 1600$. It seems reasonable, but certainly questionable, to conclude that $\xi(t,0)$ grows linearly in time. A more compelling proof of the existence of diffusion will be given later on in § 4.3.

Assuming, for the time being, that $\xi(t,0)$ is linear in t, we face the problem of determining its exact slope. This difficulty is illustrated in figure 2 which shows linear least-square fits evaluated in two different regions of the time domain. The resulting slopes are quite different, and the exact value of the diffusion coefficient seems to depend on the interval chosen to interpolate a linear fit.

This ambiguity is due to the statistical nature of Δy and, in statistical methods, is generally encountered in evaluating the variance of certain random variables. Specifically, suppose that $\psi_1 \ldots \psi_n$ are n independent Gaussian random variables with zero mean and unknown variance σ^2. The latter can be estimated by the random variable S_n, defined as

$$S_n = \frac{1}{n}\sum_{i=1}^{n}\psi_i^2. \tag{3.3}$$

Since $\langle S_n \rangle = \sigma^2$ and, from the law of large numbers, $\lim_{n\to\infty} S_n = \sigma^2$, S_n is a good estimate for the variance of ψ_i. However, S_n is not equal to σ^2 for finite n and the

https://doi.org/10.1017/S0022112001005122 Published online by Cambridge University Press

error of this estimate, i.e. the r.m.s. of S_n, can be shown to be (Folland 1984, p. 293)

$$\mathrm{Var}(S_n) = \langle \big(S_n - \langle S_n \rangle\big)^2 \rangle = 2\,\frac{\sigma^4}{n}\,. \tag{3.4}$$

In the case under consideration, we identify the ψ_i with Δy even though, strictly speaking, the particle displacements for a single configuration are generally not independent, and note that the variance σ^2 of the p.d.f. of Δy grows with t. Therefore, in order to minimize the relative error in evaluating σ^2 which, in view of (3.4) is $O(1/\sqrt{n})$, one should strive to have a large number of degrees of freedom n. But, since a single initial configuration gives, at most, $n = N$, we can increase n using a large number N_c of initial configurations so that $n = N \times N_c$. In that case we have, in lieu of (3.2),

$$\langle \xi(t,\tau) \rangle = \frac{1}{N_c} \sum_{i=1}^{N_c} \frac{1}{N} \sum_{\alpha=1}^{N} \big[y_i^\alpha(\tau + t) - y_i^\alpha(\tau) \big]^2\,, \quad \tau \geqslant 0\,, \tag{3.5}$$

where $y_i^\alpha(\tau + t)$ is the y-coordinate of particle α at time $\tau + t$ taken from the initial configuration i. Again, an alternative approach would be to take the different configurations by dividing one single long run into non-overlapping intervals. This method was tried in a few cases and gave results equivalent to those using the method of ensemble averaging.

Although all our computations were performed in the presence of the inter-particle force given by (2.1), there exists the fundamental issue of whether diffusion would still occur if this force were absent. Recall that, under the action of exclusively hydrodynamic effects, the particle configuration in the sheared suspension would evolve according to the system of the Stokes equations which are reversible as well as deterministic. The latter implies, of course, that, given the initial particle configuration at time τ, it should be possible, at least in principle, to determine exactly the positions of all the particles at time $\tau + T$. On the other hand, reversibility implies that, upon reversing the direction of shear at time $\tau + T$ one should be able to return these same particles to their initial positions at time $\tau + 2\,T$ giving $\xi(2\,T, \tau) = 0$, where ξ is defined by (3.2). Since such a result is incompatible with diffusion, one is left with the task of explaining how a macroscopic irreversibility, such as diffusion, could possibly arise in a system which is reversible on a microscale.

An analogous paradox has been known for a long time in classical statistical mechanics where the movement of a large number of molecules whose equations of motions are reversible give rise to irreversible phenomena that are described by irreversible macroscopic equations such as the Boltzmann equation (see Kreuzer 1981, for an extensive review).

In our case, the result $\xi(2\,T, \tau) = 0$ referred to above presupposes that the positions of the particles at time $\tau + T$, i.e. at the instant where the direction of the shear is reversed, are known with infinite precision. But, if for some reason, this piece of information is slightly imprecise, then the initial positions of the particles cannot be recovered. In an experiment this loss of information arises from unavoidable small irreversible effects, i.e. surface roughness, Brownian and inertial forces etc., which can never be eliminated, while, in computer simulations, it enters through round-off errors and imperfect computations.

As an illustration, consider the evolution of $\langle \xi(t,\tau) \rangle$, shown in figure 3, for $\phi = 0.35$ and with $F_0 = 10$, $\tau = 4$, and $\lambda = 10^3, 10^4, 10^5$, where $\langle \xi(t,\tau) \rangle$ is given by (3.5) with $N_c = 512$ initial hard-sphere configurations. (We have chosen to illustrate the

https://doi.org/10.1017/S0022112001005122 Published online by Cambridge University Press

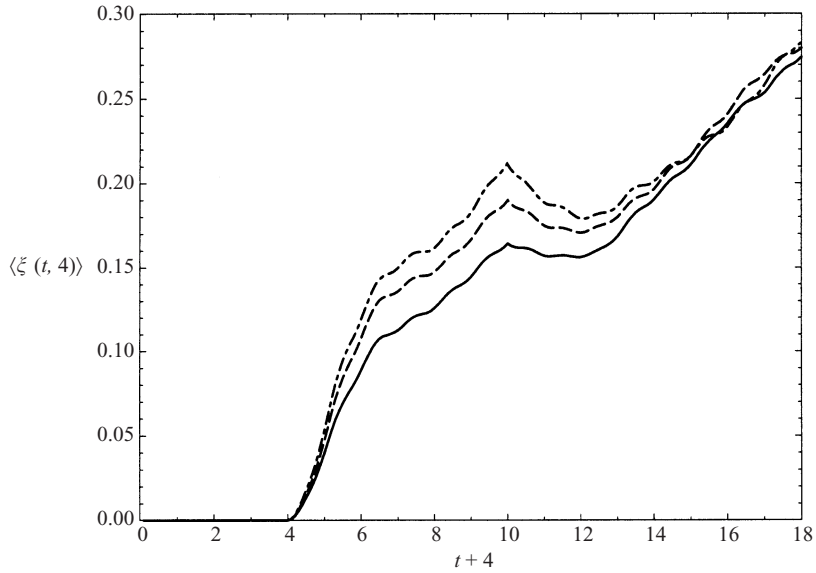


FIGURE 3. Plot of $\langle \xi(t,\tau) \rangle$ for $\phi = 0.35$ and for $\tau = 4$, $F_0 = 10$, $N_c = 512$, $\lambda = 10^3$ (solid line), 10^4 (dashed line), 10^5 (dot-dashed line). At time $t = T = 6$ the direction of the shear is reversed.

evolution of $\langle \xi(t,\tau) \rangle$ rather than that of $\xi(t,\tau)$ since the latter is both irregular and highly dependent on the particular initial hard-sphere configuration; hence the issue of reversibility cannot be probed as clearly with $\xi(t,\tau)$ as it can by examining the response of $\langle \xi(t,\tau) \rangle$ to flow reversal.) It is seen that if the direction of shear is reversed at time $\tau + T = 10$, the computed values of $\langle \xi(t,\tau) \rangle$ tend to be symmetric about $t = T = 6$ for a short time beyond this point but eventually resume growing with increasing t. The fact that the time $t + 4 = 13$ at which $\langle \xi(t,\tau) \rangle$ attains a local minimum beyond $t + 4 = 10$, was only slightly affected by choosing three very different values for the strength of the inter-particle force suggests that any small departure from reversibility will amplify at least exponentially. According to our simulations therefore, upon reversal of the direction of shear, the suspension loses its memory after a time interval of the order of one strain, and that, thereafter, the evolution of the particle configuration proceeds as if the flow reversal had never taken place. This loss of memory after a finite strain is consistent with the results of the flow reversal experiments described by Gadala-Maria & Acrivos (1980).

4. Autocorrelation time and the self-diffusion coefficients

In the previous section we showed that the p.d.f. of the particle displacements in the two transverse directions is Gaussian but that, irrespective of the length of the simulation, it is not possible to determine, from equation (3.2) starting from a single hard-sphere distribution, an unambiguous linear relationship between their average square displacements and the time t. We also deduced from equation (3.4) that, with simulations using a small number of particles, it is necessary to employ data from different configurations in order to determine the diffusion coefficients with reasonable accuracy. This approach was suggested first by Breedveld *et al.* (1998) who determined experimentally the diffusion coefficients from the p.d.f. of the particle displacements as obtained from many different configurations, and was followed by Foss & Brady

https://doi.org/10.1017/S0022112001005122 Published online by Cambridge University Press

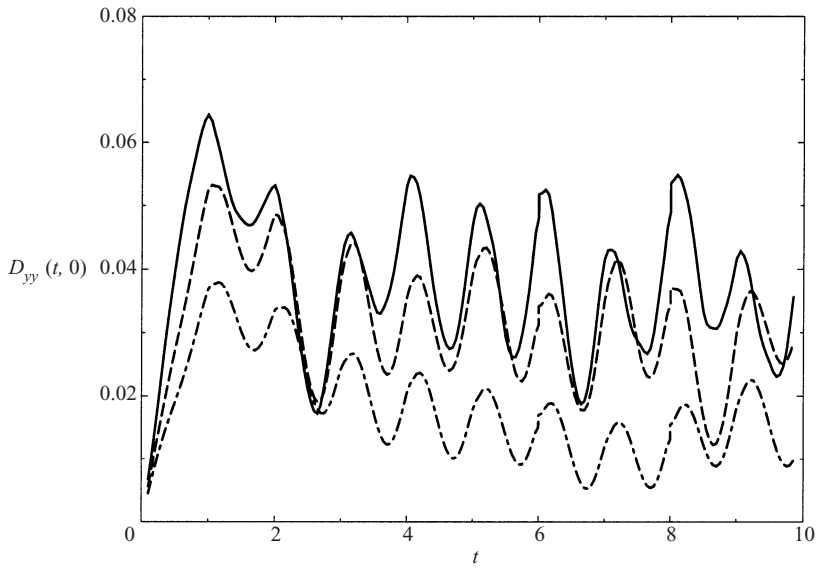


FIGURE 4. Graph of $D_{yy}(t,0)$ defined in equation (4.1) for $\phi = 0.25$ (dot-dashed line), $\phi = 0.35$ (dashed line), $\phi = 0.45$ (solid line), for $N = 27$ and $N_c = 512$.

(1999) in their computation via numerical simulations of the diffusion coefficient in the presence of Brownian forces. More precisely, let us define

$$D_{yy}(t,\tau) = \frac{1}{2}\frac{\mathrm{d}}{\mathrm{d}t}\langle \breve{\xi}(t,\tau)\rangle\,, \tag{4.1}$$

with $\langle \breve{\xi}(t,\tau)\rangle$ defined by (3.5). An analogous definition for $D_{zz}(t,\tau)$ can be obtained by substituting y with z in the definition of $\langle \breve{\xi}(t,\tau)\rangle$ in (3.5).

In order to have diffusion in the sheared suspension, it is necessary that the mean-square displacements in the y- and z-directions both grow linearly in time, in which case the long time particle self-diffusion coefficients $\hat{D}_{yy}$ in the y-direction and $\hat{D}_{zz}$ in the z-direction, are defined as the limit, respectively, of $D_{yy}(t,\tau)$ and $D_{zz}(t,\tau)$ when $t \to \infty$, these limiting values being independent of τ.

Figure 4 shows a plot of $D_{yy}(t,0)$ for $N_c = 512$, $N = 27$, and $\phi = 0.25$, 0.35, and 0.45, from which it is clear that $D_{yy}(t,0)$ does not reach a constant value for increasing t but oscillates with a period equal to precisely one for a cubic box. The data shown in figure 4 were obtained using an ensemble of initial particle configurations as generated by a hard-sphere molecular-dynamics method, in which all the particles are placed in the same cubic box but in different non-overlapping locations.

The presence of these oscillations prevents us from evaluating the limit of $D_{yy}(t,0)$, and hence the diffusivity, except in an approximate way. In order to find the cause of these oscillations, and thereby to devise a method for eliminating them, we next consider the simpler case of evaluating the intensity of the velocity fluctuations.

4.1. *Oscillations of the intensity of the velocity fluctuations*

Consider the intensity of the velocity fluctuations in the y-direction defined as

$$\langle v^2(\tau)\rangle \;= \frac{1}{N_c}\sum_{i=1}^{N_c}\frac{1}{N}\sum_{\alpha=1}^{N}\left[v_i^{\alpha}(\tau)\right]^2, \quad \text{with } \langle v(\tau)\rangle = 0, \tag{4.2}$$

https://doi.org/10.1017/S0022112001005122 Published online by Cambridge University Press

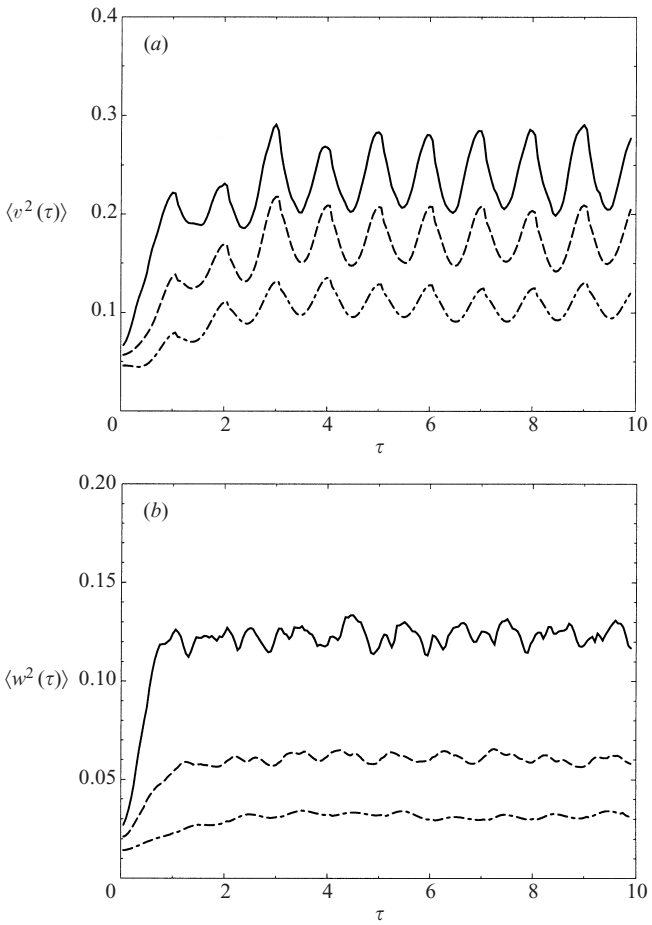


FIGURE 5. Graph of (*a*) $\langle v^2(\tau)\rangle$ defined in equation (4.2), and (*b*) $\langle w^2(\tau)\rangle$ for $\phi = 0.25$ (dot-dashed line), $\phi = 0.35$ (dashed line), $\phi = 0.45$ (solid line), for $N = 27$ and $N_c = 512$.

where $v_i^\alpha(\tau)$ is the y-component of the velocity of particle α at time τ starting from an initial hard-sphere configuration i. A plot of $\langle v^2(\tau)\rangle$ for $N_c = 512$, $N = 27$, and $\phi = 0.25$, 0.35, and 0.45, is shown in figure 5(*a*), from which it is clearly visible that $\langle v^2(\tau)\rangle$ oscillates with exactly the same period as did $D_{yy}(t, 0)$. As shown in figure 5(*b*), however, such regular oscillations were not observed in the evolution of the intensity of the z-component of the velocity fluctuations $\langle w^2(\tau)\rangle$.

To study more quantitatively this effect on the long-time behaviour, we considered the case of the evolution of a single initial configuration ($N_c = 1$) sheared for a very long time ($\tau_\infty = 6554$) and we evaluated the Fourier transform of $\langle v^2(\tau)\rangle$,

$$F_{\langle vv\rangle}(\nu) = \left| \int_0^{\tau_\infty} \mathrm{d}\tau \, \langle v^2(\tau)\rangle \, \mathrm{e}^{2\pi \mathrm{i} \nu \tau} \right| , \tag{4.3}$$

shown in figure 6 as a function of the frequency ν. Two very sharp peaks are clearly noticeable at $\nu = 0$ and at $\nu = 1$, and a smaller one at $\nu = 2$. The peak at $\nu = 0$ is due to the constant part of the signal and is not related to the oscillations, but the remaining peaks, in particular that at $\nu = 1$, refer to the anomaly under discussion. For an initially cubic shape, the simulations were repeated for a different number

https://doi.org/10.1017/S0022112001005122 Published online by Cambridge University Press

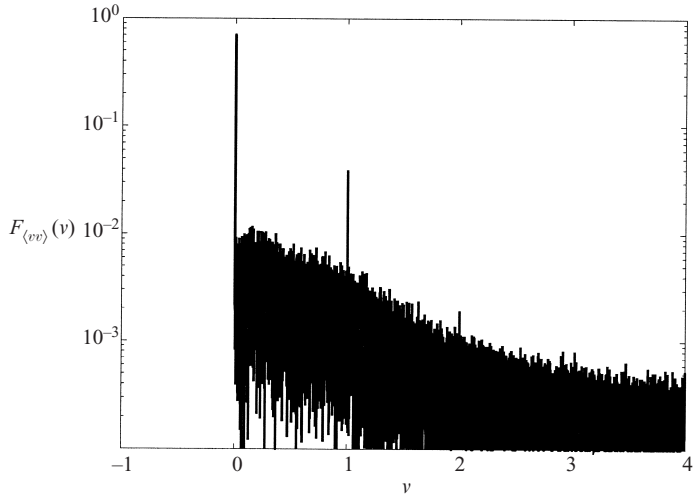


FIGURE 6. Plot of $F_{\langle vv\rangle}(v)$, the Fourier transform of $\langle v^2(\tau)\rangle$ defined in (4.3), for a cubic box with $N = 16$, $N_c = 1$, $\phi = 0.45$, and $\tau_\infty = 6554$.

Shape of the box: $L \times H$	Frequency of the highest peak beyond $v = 0$	Magnitude of the peak beyond $v = 0$
20×10	1/2	2×10^{-1}
10×10	1	4×10^{-2}
10×15	3/2	7×10^{-3}
10×20	2	2×10^{-3}

TABLE 1. Values and locations of the peaks of $F_{\langle vv\rangle}(v)$, the Fourier transform of $\langle v^2(\tau)\rangle$ defined in (4.3), in a monolayer, where L and H are, respectively, the extension of the cell in the x- and y-directions. The length of the box in the z-direction, L_z was always set equal to 10 particle radii and the areal fraction was 0.50.

of particles and different sizes of the box but the locations of the peaks remained unchanged. This procedure was then repeated for four different shapes of the initial box. The results are reported in table 1 for a monolayer of particles with areal fraction equal to 0.50, where the horizontal length and height of the boxes, denoted by L and H respectively, is listed in the first column, the location of the highest peak (not considering that at $v = 0$) in the second, and the magnitude of that peak in the third. Clearly there is a direct relation between the side–height ratio of the initial box and the location of the maximum peak.

These regular oscillations were also present when we performed simulations of the sheared suspension by neglecting the long-range interactions. This was accomplished in two independent ways: by running simulations with a code based on the method described by Ball & Melrose (1997), as well as by employing a variation of the Stokesian dynamics code in which only lubrication forces were retained. In both cases the frequency of the oscillations remained unchanged and their magnitude was comparable with that obtained from simulations in which the complete hydrodynamic interactions were retained.

It was also noticed that the regular oscillations slowly decrease in magnitude as

https://doi.org/10.1017/S0022112001005122 Published online by Cambridge University Press

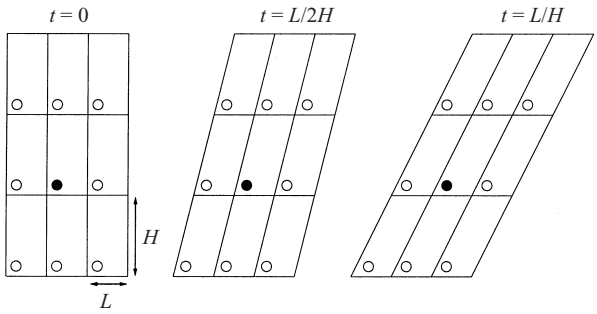


FIGURE 7. Shape of the unit cell and its images at times, $t = 0$, $L/2H$, L/H. As can be seen the configuration has the highest symmetry in the y-direction at $t = 0$ and this symmetry is recovered after a strain of L and at a frequency H/L.

the height of the cubic cell, hereby denoted by H, is increased. In order to check this dependence more quantitatively, a simulation was performed with $\phi = 0.45$ and $N = 64$ giving a side length 4/3 times bigger than that of the cubic box with 27 particles at the same volume fraction. It was found that the intensity of the oscillations relative to the mean value of v^2 was reduced from 0.32 to about 0.24, the ratio being 4/3. By assuming an inverse relation between the magnitude of the oscillations and H, we therefore conclude that to reduce the oscillations to values less than 5% of the mean it would be necessary to increase the cell side to about 6.5 times that of the box containing 27 particles. At $\phi = 0.45$, this would then require a box with more than 7000 particles, clearly far in excess of the number of particles which can be handled using currently available computer capabilities.

The regular oscillations in the intensity of the velocity fluctuations seem, therefore, to be due to a finite-size effect which, apparently, could be eliminated, for any given configuration, only by increasing the size of the box. As we shall presently show, however, the same goal can be accomplished by starting the computations with an ensemble of configurations that are randomly out of phase with each other.

4.2. *Elimination of the regular oscillations*

To understand the nature of the regular oscillations one has to consider the details of the numerical simulations from which they arise. To ensure the correct representation of long-range interaction with a finite number of particles, Brady *et al.* (1988) have shown that it is necessary to confine the particles in a periodic lattice. At this point, the only way to apply a shear in a dynamic way is by means of the Lees–Edwards boundary conditions, see e.g. Allen & Tildesley (1987, p. 246), in which the shape of the lattice changes and deforms in time until it reaches the original cubic lattice shape (that is with exactly the same frequency as that indicated in table 1). Consequently, a spurious periodicity is introduced into the hydrodynamic calculations by the instantaneous shape of the lattice. This is illustrated in figure 7 where we show the instantaneous shape of the unit cell and its images at times $t = 0, L/2H, L/H$. As can be seen, the configuration has the highest symmetry in the y-direction at $t = 0$ and this symmetry is recovered after a strain of L and at a frequency H/L. On the other hand, the shape of the box in the z-direction is not altered, a fact which accounts for the lack of any observed regular oscillations in $\langle w^2(\tau)\rangle$.

Other observations support the argument that the regular oscillations originate from the periodic evolution of the cell shape. The first pertains to the fact that these oscillations cannot be filtered out by averaging over the initial configurations even

https://doi.org/10.1017/S0022112001005122 Published online by Cambridge University Press

though the latter are unrelated to each other. This implies that all configurations have not only the same frequency but the same phase as well. The second refers to the fact that these oscillations are very persistent, and show no measurable decay in their amplitude. Thirdly, the decrease of the amplitude of the regular oscillations with increasing H shows that this phenomenon loses its importance when the periodic boundary condition in y no longer plays a dominant role in shaping the evolution of the particle configuration. Finally, as we shall presently show, our assumption regarding the origin of the oscillations is also consistent with the fact that these can be effectively eliminated by randomly averaging over the orientation of the initial shape of the periodic lattice, which is equivalent to averaging over the initial time t_0, with t_0 ranging from 0 to 1 for a cubic box.

Guided by the results plotted in figure 5 we therefore take it for granted that, when $\tau \gg 1$, $\langle v^2(\tau)\rangle$ can be represented by

$$\langle v^2(\tau)\rangle = A^2 + B\,\mathrm{e}^{2\mathrm{i}\pi\nu\tau} \quad \text{for } \tau \gg 1, \tag{4.4}$$

where A and B are time independent and $\nu = 1$ for a cubic box.

In order to eliminate the regular oscillations, it suffices then to introduce a random phase in the time of each single configuration by starting each simulation from a random negative time, so that equation (4.4) now becomes

$$\langle v^2(\tau)\rangle = A^2 + B\,\mathrm{e}^{2\mathrm{i}\pi\nu(\tau+\eta)}, \tag{4.5}$$

where η is a random number, ranging from 0 to 1 for a cubic box, independent of the initial configurations and the average is taken only over those configurations for which η lies between η and $\eta + \mathrm{d}\eta$. Further averaging over η yields

$$\langle\langle v^2(\tau)\rangle\rangle = A^2 \quad \text{for } \tau \gg 1, \tag{4.6}$$

which no longer contains the effects of the regular oscillations given that $\langle \mathrm{e}^{2\mathrm{i}\pi\nu\eta}\rangle = 0$. This procedure is equivalent to changing the definition of the average from that of (4.2) to

$$\langle\langle v^2(\tau)\rangle\rangle = \frac{1}{N_c}\sum_{i=1}^{N_c}\frac{1}{N}\sum_{\alpha=1}^{N}\left[v_i^{\alpha}(\tau+\eta_i)\right]^2, \tag{4.7}$$

where η_i is a random number for each configuration uniformly distributed between 0 and 1 for a cubic box. As shown in figure 8, which depicts a plot of $\langle\langle v^2(\tau)\rangle\rangle$ obtained using the procedure of randomized phases just described, the large regular oscillations have disappeared. Also, the remaining noise can be made as small as desired by increasing the number of configurations. We wish to remark parenthetically that the method which we have devised for the purpose of eliminating these regular oscillations is by no means unique in that any number of filtering techniques could have been employed for achieving the same goal. Our method has the great advantage, however, that it can be applied simultaneously to the computation of all the physical quantities of interest, such as the displacements, the velocities, and the velocity autocorrelation functions. We also wish to point out that, if the regular oscillations seen in figures 4 and 5(*a*) were physical, e.g. due to the formation and destruction of clusters, rather than spurious as we have assumed, it would not have been possible to remove them just by shifting the origin of time in the initial hard-sphere configurations.

In what follows, we shall use the definitions of the averages similar to (4.7) and proceed to describe the calculation of the different coefficients characterizing the sheared suspension.

https://doi.org/10.1017/S0022112001005122 Published online by Cambridge University Press

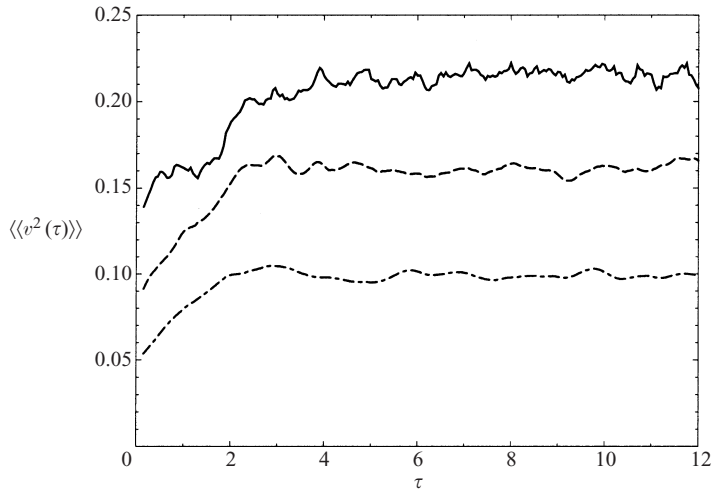


FIGURE 8. Graph of $\langle\langle v^2(\tau)\rangle\rangle$ as defined in equation (4.7), for $\phi = 0.25$ (dot-dashed line), $\phi = 0.35$ (dashed line), $\phi = 0.45$ (solid line), for $N = 16$ and $N_c = 512$.

N	N_c	$1/H$	$\hat{D}_{yy}$	$\tilde{D}_{yy}$	$\hat{D}_{zz}$	$\tilde{D}_{zz}$
16	512	0.1735	0.019 ± 0.003	0.019 ± 0.003	0.009 ± 0.001	0.008 ± 0.001
27	256	0.1457	0.027 ± 0.003	0.025 ± 0.006	0.012 ± 0.001	0.012 ± 0.001
54	32	0.1157	0.037 ± 0.012	0.038 ± 0.020	0.014 ± 0.006	0.012 ± 0.008
64	32	0.1093	0.038 ± 0.009	0.037 ± 0.025	0.015 ± 0.004	0.013 ± 0.008
∞		0	0.041 ± 0.007	0.037 ± 0.013	0.016 ± 0.002	0.017 ± 0.003

TABLE 2. Values of the self-diffusivities evaluated for a volume fraction $\phi = 0.35$. N is the number of particles in the unit cubic cell, N_c is the number of configurations in the ensemble, and H is the height of the cell. The values for $1/N = 0$ were obtained by a linear extrapolation.

4.3. *Numerical results for the self-diffusivities*

We now return to the problem of establishing the diffusive behaviour of the sheared suspension. To avoid the oscillations of figure 4, we evaluated $D_{yy}(t, \tau)$ from equation (4.1) using, for one-half the average square displacement, the definition

$$\langle\langle \xi(t,\tau)\rangle\rangle = \frac{1}{N_c}\sum_{i=1}^{N_c}\frac{1}{2N}\sum_{\alpha=1}^{N}\left[y_i^\alpha(\tau + t + \eta_i) - y_i^\alpha(\tau + \eta_i)\right]^2, \tag{4.8}$$

in lieu of (3.5). An analogous definition holds for one-half the average square displacement in the z-direction. A plot of $D_{yy}(t, 0)$ as obtained using both definitions (4.8) and (3.5), for 27 particles, with $N_c = 512$, $\phi = 0.15$, is given in figure 9. In the limit of large t, in the particular case of this figure for $t \geqslant 8$, $D_{yy}(t, 0)$, as obtained from (4.1) and (4.8), approaches a constant value so that, in contrast to using (3.5), the self-diffusion coefficient $\hat{D}_{yy}$ can now be determined. An analogous result applies for $\hat{D}_{zz}$ which, however, can be computed using either (3.5) or (4.8), since there are no regular oscillations in the z-direction.

In table 2, we report the computed values of the self-diffusivity both in the y- and z-directions, for a volume fraction $\phi = 0.35$, as obtained with a different number of particles in the unit cell, $N = 16$, 27, 54, and 64 with the reported error being

https://doi.org/10.1017/S0022112001005122 Published online by Cambridge University Press

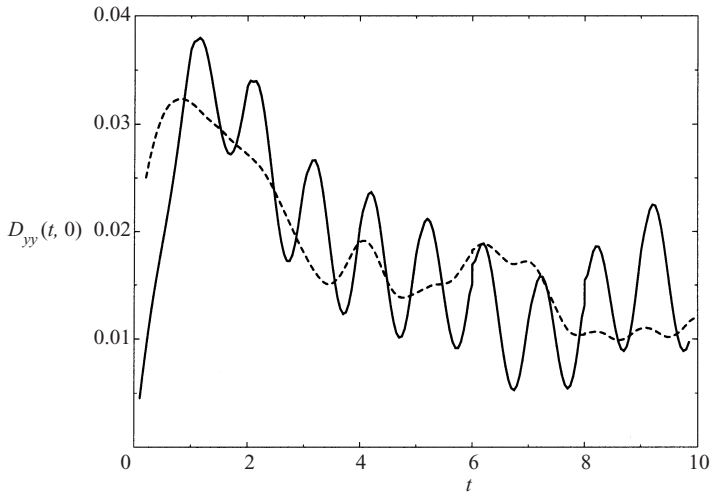


FIGURE 9. Graph of $D_{yy}(t,0)$, as defined in (4.1), where the average displacements are defined as in (3.5) (solid line) and in (4.8) (dashed line), $N = 27$, $N_c = 512$, $\phi = 0.15$.

the r.m.s. obtained from the ensemble average. Clearly, the computed self-diffusion coefficients depend on the number of particles used in the simulations. Guided by the results of simulations recently reported by A. Sierou & J. F. Brady (2000, personal communication), who used several hundred particles, we therefore expressed $\hat{D}_{yy}$ and $\hat{D}_{zz}$ as linear functions of $1/N$ and, by means of a least-squares regression analysis, extrapolated the values of these diffusivities to $N \to \infty$. Figure 10 shows a comparison of the extrapolated values of (*a*) $\hat{D}_{yy}$ and (*b*) $\hat{D}_{zz}$, with previous experimental and numerical results. For volume fractions below 0.30 there is fair agreement with the data in the literature but, for more concentrated suspensions, such a comparison is less satisfactory. Consistent with the experimental data, however, our computed values of $\hat{D}_{yy}$ are significantly higher than those of $\hat{D}_{zz}$ at the same volume fraction. Nevertheless, several discrepancies are clearly evident in figure 10, which require further study.

4.4. *Numerical results for the autocorrelation function*

We next consider the correlation between the transverse velocity of a certain particle at two different times, also known as the velocity autocorrelation function. The evaluation of this function for the velocity in the y-direction, using the random-phase adjustment to avoid the regular oscillations, is done using

$$\langle\langle v(\tau + t)v(\tau)\rangle\rangle = \frac{1}{N_c}\sum_{i=1}^{N_c}\frac{1}{N}\sum_{\alpha=1}^{N} v_i^{\alpha}(t + \tau + \eta_i)\, v_i^{\alpha}(\tau + \eta_i), \tag{4.9}$$

where $v_i^{\alpha}(t)$ is the y-component of the velocity of particle α at time t in the configuration i, and η_i is a random number between 0 and 1 for a cubic box; the autocorrelation function in the z-direction has a similar definition with v replaced by w. A typical graph of $\langle\langle v(\tau + t)v(\tau)\rangle\rangle$, normalized by $\langle\langle v^2(\tau)\rangle\rangle$, is shown in figure 11(*a*), for $\tau = 5$, $N_c = 256$, $N = 27$, $\phi = 0.35$ and 0.45. We notice that the autocorrelation function quickly drops to zero after about 0.8 strains, remains negative for about four strains, and then becomes negligible shortly thereafter. A similar qualitative behaviour is obtained at different volume fractions or with a different number of particles. The

https://doi.org/10.1017/S0022112001005122 Published online by Cambridge University Press

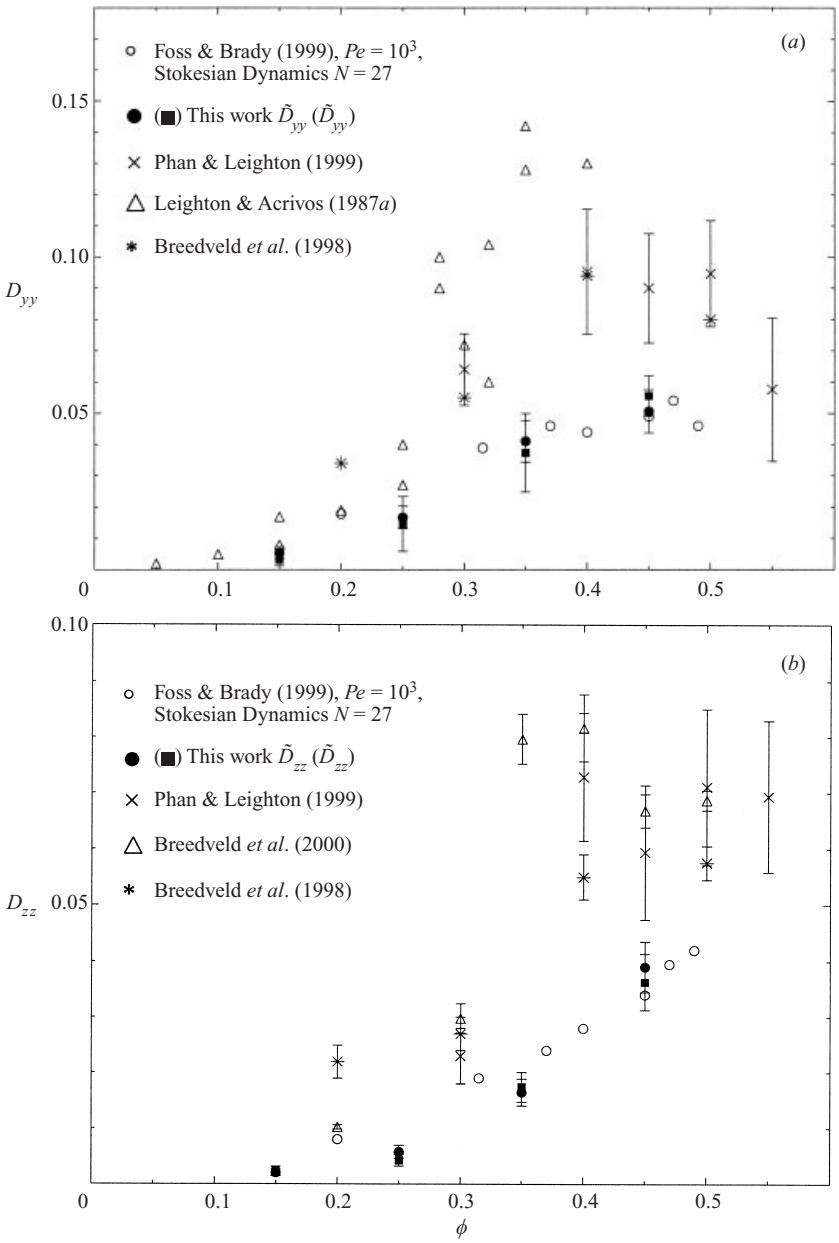


FIGURE 10. Comparison of (*a*) the *yy*-component and (*b*) the *zz*-component of the long-time self-diffusion tensor extrapolated to $1/H = 0$ with earlier experiment and computational results.

presence of a long tail in $\langle\langle v(\tau + t)v(\tau)\rangle\rangle$ suggests that, even though the velocity auto-correlation becomes very small (less than 20%) within one strain, a much longer time is required, about four or five strains for the particular case of figure 11(*a*), for the suspension to evolve into a completely independent state. The autocorrelation function for the velocity in the *z*-direction, shown in figure 11(*b*), has a similar qualitative behaviour.

Knowledge of the autocorrelation function also allows us to calculate the self-

https://doi.org/10.1017/S0022112001005122 Published online by Cambridge University Press

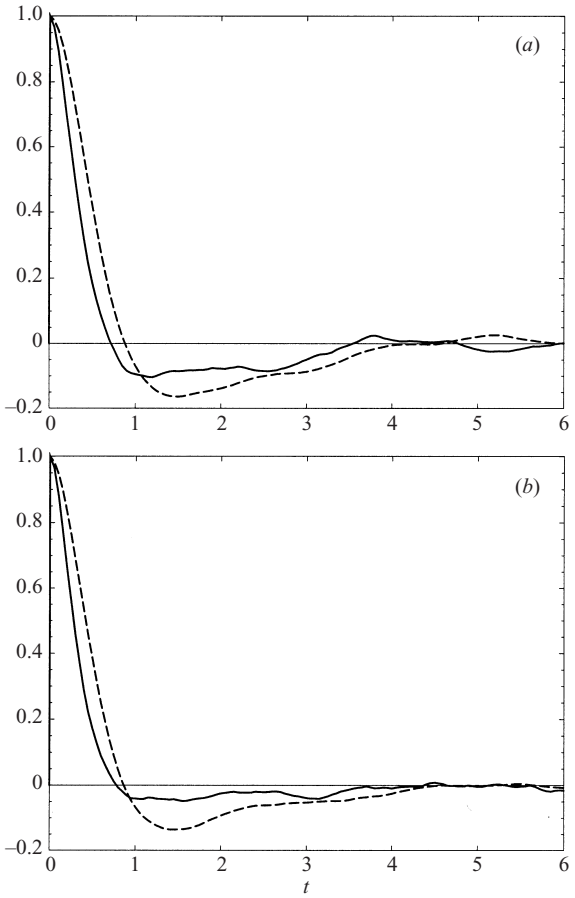


FIGURE 11. Autocorrelation functions for the velocity (*a*) *y*-component and (*b*) *z*-component, normalized by their respective values at $t = 0$, for $\tau = 5$, $N = 27$, and $\phi = 0.35$ (dashed lines), $\phi = 0.45$ (solid lines).

diffusion coefficient in an independent way using the well-known expression (for details, see Berne & Pecora 1976, p. 86)

$$\langle\langle \xi(t,\tau)\rangle\rangle \equiv \frac{1}{2}\frac{\mathrm{d}}{\mathrm{d}t}\langle\langle [y(\tau+t)-y(\tau)]^2\rangle\rangle = \int_0^t \langle\langle v(\tau+t')v(\tau)\rangle\rangle \,\mathrm{d}t'\,. \tag{4.10}$$

Therefore,

$$\tilde{D}_{yy} = \int_0^\infty \lim_{\tau\to\infty} \langle\langle v(\tau+t)v(\tau)\rangle\rangle \,\mathrm{d}t\,, \tag{4.11}$$

and similarly for the coefficient $\tilde{D}_{zz}$ in the z-direction. Values for $\tilde{D}_{yy}$ and $\tilde{D}_{zz}$ for $\phi = 0.35$, as obtained from equation (4.11) with $N = 16$, 27, 54, and 64, are reported in table 2, where the indicated error is the r.m.s. of the ensemble average. The values of the diffusivities from the average square displacements and from the integral of the autocorrelation function are also essentially equal to each other for the other volume fractions considered, but are not printed here. We notice that, for the same number of configurations, the error in the evaluation of $\hat{D}_{yy}$ and $\hat{D}_{zz}$ is consistently smaller than that of $\tilde{D}_{yy}$ and $\tilde{D}_{zz}$.

https://doi.org/10.1017/S0022112001005122 Published online by Cambridge University Press

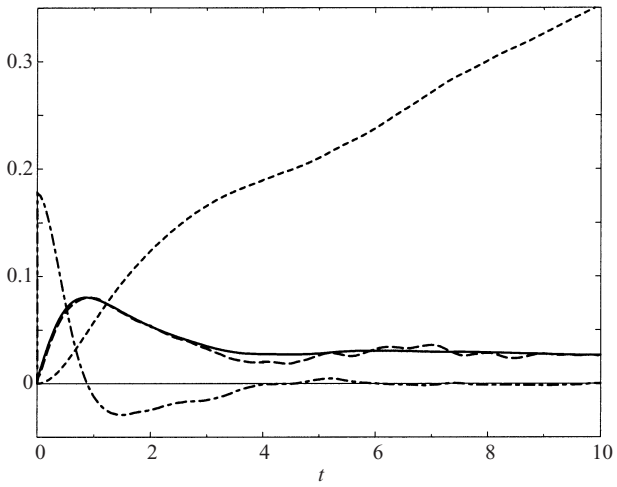


FIGURE 12. A plot of $\langle\langle v(t+\tau)v(\tau)\rangle\rangle$ (dot-dashed line), together with its integral (solid line), also $D_{yy}(t,\tau)$ (dashed line), and $\langle\langle\xi(t,\tau)\rangle\rangle \equiv \frac{1}{2}\langle\langle[y(t+\tau)-y(\tau)]^2\rangle\rangle$ (dotted line), for $N_c = 512$, $N = 27$, $\phi = 0.35$, $\tau = 5$.

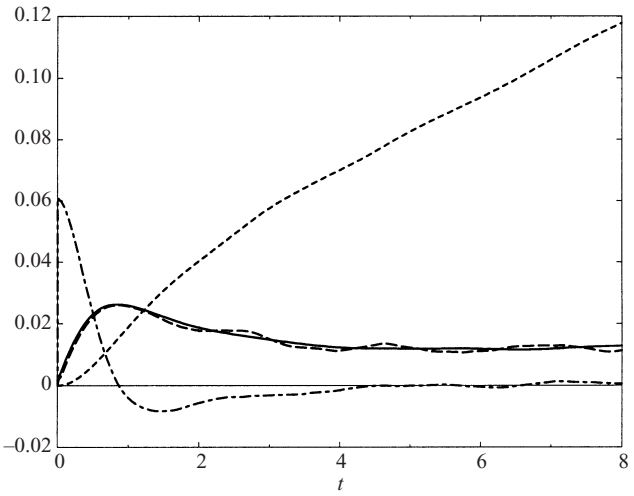


FIGURE 13. A plot of $\langle\langle w(t+\tau)w(\tau)\rangle\rangle$ (dot-dashed line), together with its integral (solid line), also $D_{zz}(t,\tau)$ (dashed line), and $\frac{1}{2}\langle\langle[z(t+\tau)-z(\tau)]^2\rangle\rangle$ (dotted line), for $N_c = 512$, $N = 27$, $\phi = 0.35$, $\tau = 5$.

Shown in figure 12 is a comparison between $\int_0^t\langle\langle v(\tau+t')v(\tau)\rangle\rangle \mathrm{d}t'$ (plotted as a solid line) and $D_{yy}(t)$, the dashed line from equations (4.1) and (4.8), which are seen to be equal within numerical error. This same degree of agreement was also found in all the other cases which were considered. An analogous comparison for the components in the z-direction is also shown in figure 13, where the curves are seen to be very similar to those of figure 12.

The form of $\langle\langle v(\tau+t)v(\tau)\rangle\rangle$ and the relation (4.10) just verified allow us to understand more fully the dependence of $\langle\langle\xi(t,\tau)\rangle\rangle$ on t (plotted as a dotted line in figures 12 and 13). For $t \to 0$, this quantity grows quadratically,

$$\tfrac{1}{2}\langle\langle\xi(t,\tau)\rangle\rangle \simeq \langle\langle v^2(\tau)\rangle\rangle\, t^2 \quad \text{as } t \to 0, \tag{4.12}$$

https://doi.org/10.1017/S0022112001005122 Published online by Cambridge University Press

N	N_c	0.15	0.25	0.35	0.45
16	512	8.6	5.4	4.1	2.9
27	256	6.5	5.3	3.5	3.0
54	32	8.5	5.0	3.2	3.1
64	32	6.5	4.8	4.7	3.2

TABLE 3. Values of the correlation time T_c, defined by equation (4.13), for $\phi = 0.15$, 0.25, 0.5, and 0.45, N is the number of particles in the unit cell, N_c the number of configurations in the ensemble.

as confirmed by the numerical results. Thus, at these time scales the motion is not diffusive. This constitutes a very important difference between the suspension considered here, in which Brownian motion is neglected, and a suspension at finite Péclet numbers where the short-time diffusivities are independent of t and proportional to the mobility matrix (see e.g. Brady 1994). Moreover, in our case, an apparently linear regime is reached in the range $0.5 < t < 2$ due to the fact that the autocorrelation function changes sign at about $t = 1$ where its integral reaches a local extremum. This led some earlier researchers, e.g. Foss & Brady (1999), to terminate their simulations at $t = 2$ in the mistaken belief that they had reached the asymptote for the diffusion coefficient. Finally, for $t > 5$ we have $\langle\langle v(\tau + t)v(\tau)\rangle\rangle \simeq 0$, so that its integral, $D_{yy}(t)$, becomes constant and the final diffusive steady state is reached. More precisely, for any large τ, e.g. $\tau > 5$, let us define the *correlation time* as the smallest time T_c such that

$$\frac{|\langle\langle v(\tau + t)v(\tau)\rangle\rangle|}{\langle\langle v^2(\tau)\rangle\rangle} \leqslant 0.05 \quad \text{for any } t \geqslant T_c. \tag{4.13}$$

This correlation time is an important time scale for the flow of the suspension, in that it refers to the time interval which must be exceeded before the average particle square displacement can be described with a diffusion equation. In table 3 we report the correlation times found from our numerical simulations for different number of particles in the unit cell and different values of the volume fraction ϕ. Although the evaluation of the correlation time is evidently subject to large error, its order of magnitude at various volume fractions is of some importance. As expected intuitively, T_c decreases with increasing volume fractions and its value does not seem to depend strongly on the number of particles used in the unit cell. Also, the fact that T_c is significantly larger than unity, especially at lower particle volume fractions, raises doubts regarding the accuracy of the diffusion coefficients reported by Breedveld *et al.* (1998, 2000), and shown in figure 10, because, on account of the large scatter in their data, their measured mean-square particle displacements are reliable only for values of the strain below about 0.7 and 2, respectively, both of which are smaller than T_c.

In the previous section we showed how the displacements, in the directions normal to the flow, of the position of a tagged particle in a uniform sheared suspension have a Gaussian distribution, whereas in this section we showed that, for times greater than the correlation times reported in table 3, the average square displacements grow linearly with t giving well-defined diffusion coefficients. These results were obtained with simulations involving a relatively small number of particles but, using ensemble averages. We wish to note that the main advantage of starting our simulations using initial hard-sphere configurations is that the sequence in which the suspension flow is computed for the different configurations is immaterial. This is very advantageous

https://doi.org/10.1017/S0022112001005122 Published online by Cambridge University Press

if a parallel machine or a cluster of machines is available. On the other hand, if only a single processor computer is available and the time required for $\langle\langle v^2(\tau)\rangle\rangle$ to reach its equilibrium steady state for a simple shear flow is larger than the correlation time, it may be preferable to obtain the different configurations of the ensemble by dividing a single simulation performed over a long time into many small parts and then proceeding as if these configurations were independent.

5. Evaluation of the gradient diffusivity

Up to this point we have only dealt with suspensions that are homogeneous on a macroscale, and have determined some of the key parameters that result in the presence of simple shear, e.g. the shear-induced tracer diffusivities along and normal to the plane of shear, the corresponding velocity autocorrelations functions, the *correlation time* beyond which the suspension loses its memory etc. Most practical applications, however, involve suspensions in which the particle concentration profile is non-uniform with the result that a shear-induced particle flux is created from regions of high concentrations to low (Acrivos 1995). The key parameters here are the so-called gradient diffusivities $D_{\parallel}$ and $D_{\perp}$ (Leighton & Acrivos 1987*b*), which appear in the linear relation between the particle flux $\boldsymbol{J}$ and the local particle concentration gradient in the two directions normal to the flow,

$$J_y = -D_{\parallel}\frac{\partial \phi}{\partial y} \quad \text{and} \quad J_z = -D_{\perp}\frac{\partial \phi}{\partial z}. \tag{5.1}$$

The evaluation of these two coefficients will be the subject of the remaining part of this paper.

5.1. *Non-uniform suspension*

In principle, this gradient diffusivity in one of the transverse directions, say y, could be computed by artificially introducing into the suspension a finite force F_y, periodic in y with period $2\pi/H$, and then determining via simulations how an initially statistically *homogeneous* suspension evolves under shear into a state in which the local particle concentration is also periodic in y. It can be shown that the relaxation time for this process equals $H^2/4\pi^2 D$ where D is the corresponding gradient diffusivity. The difficulty with this approach is that the simulations must be performed on suspensions which are statistically non-homogeneous. Also, since the value of D thereby obtained depends on the strength of this artificial force, the computations would have to be repeated for different values of this strength and the results extrapolated to zero.

In contrast, in the technique which we shall present below and which is a modification of that described by Marchioro *et al.* (2000, 2001), all the computations are performed on a suspension which is statistically homogeneous. The essence of this method, which has some common features with the familiar technique of determining the diffusivity of Brownian particles from light scattering experiments (Rallison & Hinch 1986), is to create a small artificial inhomogeneity in the suspension, not by altering the particle trajectories in response to an applied force, but rather by changing the probability of the different configurations in a prescribed way according to the instantaneous state of inhomogeneity. (An important difference between the two techniques will be pointed out later on in this section.)

We begin by recalling that the local ensemble-average volume fraction of the particles at location y, averaged over x and z, is given by (for a cubic cell of

https://doi.org/10.1017/S0022112001005122 Published online by Cambridge University Press

height H)

$$\phi(y,t) = \sum_{i=1}^{N_c} P(i,t) \frac{1}{H^2} \sum_{\alpha=1}^{N} \frac{4\pi}{3} \delta(y - y_i^\alpha), \tag{5.2}$$

where $P(i,t)$, to be specified more precisely later, is the probability of the configuration labelled i ($i = 1, \ldots, N_c$), $4\pi/3$ is the volume of each sphere of unit radius, and δ is the Dirac delta function. An important point which must be kept in mind is that the specification of $P(i,t)$ for any given ensemble of configurations is arbitrary and that the specific expression chosen for $P(i,t)$ will determine the properties of the system and, according to the definition (5.2), the volume fraction profile $\phi(y,t)$ within the suspension.

Specifically, let us consider a particular choice of $P(i,t)$, namely $P_0(i,t)$, which gives rise to a homogeneous suspension where, in this context, we say that the suspension is homogeneous with respect to P in the y-direction if the value of $\phi(y,t)$ is the same for each y. Now if the N_c initial configurations are sampled from a hard-sphere distribution, then there is no reason to give a higher or lower probability to any of these initial configurations, and hence, $P_0(i,0) = 1/N_c$. We also established in § 3, however, that when the simple shear is applied to any of these initial configurations in the absence of an external force, the particles will be displaced in the + or − directions with equal probability (and similarly with respect to z). As a consequence, the different configurations will maintain the same relative probability and the choice $P_0(i,t) = 1/N_c$ for every $t \geqslant 0$ will give rise to a uniform distribution.

To obtain a non-uniform system it is therefore necessary to use a different definition of $P(i,t)$. Several choices are possible but a very convenient one (see e.g. Marchioro *et al.* 2000) is to define a probability $P_\varepsilon(i,t)$, according to

$$P_\varepsilon(i,t) = P_0(i,t)\,[1 + \varepsilon\,\sigma(i,t)]\,, \tag{5.3}$$

where

$$\sigma(i,t) = \sum_{\alpha=1}^{N} \sin k\, y_i^\alpha(t)\,, \tag{5.4}$$

ε is a small parameter which, as will be seen presently, cancels out of the analysis and $k = 2\pi/H$ is such that $\sin k\, y$ is periodic over the height of the box.

The volume fraction ϕ, defined in (5.2) with P replaced by P_ε, can be expanded in a Fourier series in the spatial coordinate to give

$$\phi(y,t) = \phi_0\,[1 + S(t)\,\varepsilon \sin k\, y + R(t)\,\varepsilon \cos k\, y]\,, \tag{5.5}$$

where $\phi_0 = 4\pi N/3V$, with $V \equiv H^3$ being the volume of the cubic cell, is the homogeneous volume fraction while

$$S(t) = \frac{2}{N} \sum_{i=1}^{N_c} P_0(i,t)\,[\sigma(i,t)]^2\,, \tag{5.6}$$

and

$$R(t) = \frac{2}{N} \sum_{i=1}^{N_c} P_0(i,t) \sum_{\alpha=1}^{N} \sin k\, y_i^\alpha(t) \sum_{\beta=1}^{N} \cos k\, y_i^\beta(t)\,. \tag{5.7}$$

We shall presently show, however, that $R(t) = 0$ when the suspension described by P_0 is homogeneous and a sufficiently large number of configurations are used in the

https://doi.org/10.1017/S0022112001005122 Published online by Cambridge University Press

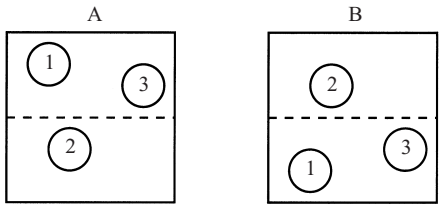


FIGURE 14. Two equally likely configurations in the homogeneous ensemble. Configuration B is obtained from A by a mirror symmetry about the centreline.

ensemble. To this end consider a possible configuration in the homogeneous ensemble, for example that labelled A in figure 14. In the ensemble another configuration, B in our example, might be present which is obtained from A by mirror symmetry about the centreline. Because of symmetry,

$$\sin k\, y_A^\alpha = -\sin k\, y_B^\alpha\,, \qquad \cos k\, y_A^\alpha = \cos k\, y_B^\alpha\,, \tag{5.8}$$

for $\alpha = 1,\ldots,N$. But since the ensemble is homogeneous, configurations A and B will have the same probability, i.e. $P_0(i_A,t) = P_0(i_B,t)$, and therefore, from equation (5.7), $R(t)$ will vanish.

The ensemble average of the particle velocity in the y-direction is defined in a way similar to equation (5.2):

$$\overline{v(y,t)} = \frac{1}{\phi(y)} \sum_{i=1}^{N_c} P_\varepsilon(i,t) \sum_{\alpha=1}^{N} \frac{4\pi}{3}\, \delta(y - y_i^\alpha)\, v_i^\alpha(t)\,, \tag{5.9}$$

where v_i^α is the velocity of particle α in the y-direction in configuration i. It is however more convenient to expand $\phi(y,t)\overline{v(y,t)}$, rather than $\overline{v(y,t)}$, in a Fourier series giving

$$\phi(y,t)\overline{v(y,t)} = \phi_0 \left[v^0(t) + v^s(t)\,\varepsilon \sin k\, y + v^c(t)\,\varepsilon \cos k\, y\right]\,, \tag{5.10}$$

where

$$v^0(t) = \sum_{i=1}^{N_c} P_0(i,t) \frac{1}{N} \sum_{\alpha=1}^{N} v_i^\alpha(t), \tag{5.11}$$

$$v^s(t) = \sum_{i=1}^{N_c} P_0(i,t)\sigma(i,t) \frac{2}{N} \sum_{\alpha=1}^{N} v_i^\alpha(t) \sin k\, y_i^\alpha(t), \tag{5.12}$$

$$v^c(t) = \sum_{i=1}^{N_c} P_0(i,t)\sigma(i,t) \frac{2}{N} \sum_{\alpha=1}^{N} v_i^\alpha(t) \cos k\, y_i^\alpha(t). \tag{5.13}$$

The parameter $v^0(t)$ is simply the average velocity of the particles in the y-direction in the homogeneous suspension (i.e. when $\varepsilon = 0$) and therefore vanishes in a shear flow. To show that v^s also vanishes, consider a possible configuration of the ensemble, for example configuration C of figure 15. Since the ensemble is homogeneous and representative of the whole configuration space, there exists another configuration, D in the example of figure 15, that can be obtained from C by a rotation of π radians. As a consequence of the symmetry of the two configurations, for each $\alpha = 1,\ldots,N$ we have

$$\sin k\, y_C^\alpha = -\sin k\, y_D^\alpha \quad \text{and} \quad v_C^\alpha = -v_D^\alpha\,. \tag{5.14}$$

The two configurations also have the same probability in the homogeneous distribu-

https://doi.org/10.1017/S0022112001005122 Published online by Cambridge University Press

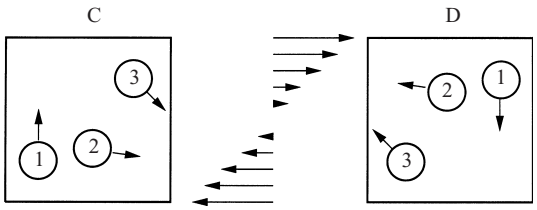


FIGURE 15. Two configurations that have the same probability in the homogeneous ensemble. Configuration D can be obtained from C by a rotation of 180°. Notice how the velocity of the particles in the vertical direction are opposite to each other in the two configurations.

tion and therefore $v^s = 0$ on account of equation (5.12). Note that the same argument does not lead to any conclusion regarding v^c because

$$\cos k\, y_C^\alpha = \cos k\, y_D^\alpha\,. \tag{5.15}$$

Next, we derive a relation between $S(t)$ and $v^c(t)$ given by equations (5.6) and (5.13), respectively, by taking the time derivative of $S(t)$, denoted by $\dot{S}(t)$, thereby obtaining

$$\dot{S}(t) = \sum_{i=1}^{N_c} P_0(i,t)\, 2\,\sigma(i,t) \frac{2}{N} \sum_{\alpha=1}^{N} \frac{\mathrm{d}}{\mathrm{d}t} \sin k\, y_i^\alpha(t) = 2\,k\, v^c(t)\,. \tag{5.16}$$

Note that in the same way one could obtain $\dot{R} = 2\,k\,v^s$, showing that $v^s = 0$ from $R = 0$. Consequently, on making use of the above together with equations (5.5) and (5.10), we find that

$$\phi(y,t) = \phi_0 + \phi_0\, S(t)\, \varepsilon \sin k\, y, \tag{5.17}$$

$$\overline{v(y,t)} = \frac{1}{2\,k} \dot{S}(t)\, \varepsilon\, \cos k\, y + O(\varepsilon^2). \tag{5.18}$$

5.2. *Flux balance and numerical results*

Before proceeding with the non-stationary case, let us consider the system at steady state. After the suspension has been sheared for a long time, the concentration profile becomes

$$\phi_\infty(y) = \phi_0 + \phi_0\, S_\infty\, \varepsilon \sin k\, y\,, \tag{5.19}$$

where $S_\infty = \lim_{t\to\infty} S(t)$. To maintain this concentration profile which has a gradient in the y-direction, it is necessary to have a time-independent flux of particles J_∞, that counterbalances the gradient diffusion flux thereby generated. Hence, by virtue of equation (5.1), this flux must satisfy

$$J_\infty \;=\; D_\parallel(\phi_\infty) \frac{\partial \phi_\infty}{\partial y} \;=\; \phi_0\, k\, D_\parallel(\phi_0)\, S_\infty\, \varepsilon\, \cos k\, y + O(\varepsilon^2)\,, \tag{5.20}$$

which also defines $D_\parallel$. In other words, the introduction of the artificial probability $P_\varepsilon(i,t)$ given by (5.3) and (5.4) is equivalent to introducing a flux along y proportional to $\cos k\, y$ that, at steady state, counterbalances the gradient diffusion flux due to the non-uniform particle concentration which $P_\varepsilon(i,t)$ has created. Moreover, since the expression for $P_\varepsilon(i,t)$ does not depend explicitly on t, we shall retain (5.20) as representing this probability-induced flux for all $t \geqslant 0$.

In the general non-stationary case, the total flux of particles crossing each plane at

https://doi.org/10.1017/S0022112001005122 Published online by Cambridge University Press

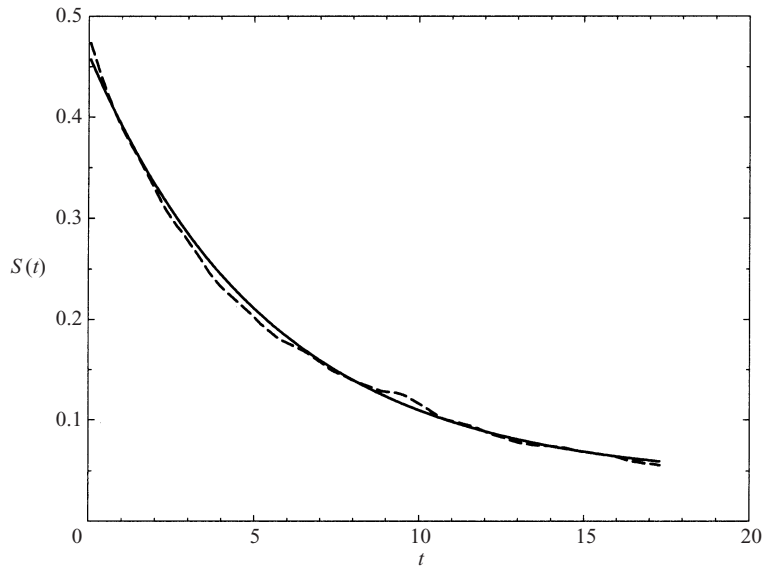


FIGURE 16. Computed values of $S(t)$ (dashed line) for $N_c = 256$, $N = 27$, $k = 0.9956$, and a volume fraction $\phi = 0.35$. The solid line, $y = 0.041 + 0.42\,\mathrm{e}^{-0.181\,t}$, is a curve fit of $S(t)$ according to (5.24).

constant y is given by

$$J^t = \phi\,\bar{v} = \frac{\phi_0}{2k}\dot{S}(t)\,\varepsilon\,\cos k\,y + O(\varepsilon^2)\,. \tag{5.21}$$

This flux is balanced by two terms: the shear-induced gradient flux given by

$$J^g \equiv -D_{\parallel}(\phi)\frac{\partial \phi}{\partial y} = -\phi_0\,k\,D_{\parallel}(\phi_0)\,S(t)\,\varepsilon\,\cos k\,y + O(\varepsilon^2)\,, \tag{5.22}$$

and the flux J_∞ defined in equation (5.20) created by $P_\varepsilon(i,t)$. Particle conservation requires that $J^t = J^g + J_\infty$, hence

$$\frac{1}{2k}\dot{S}(t) = -D_{\parallel}\,k\,[S(t) - S_\infty] + O(\varepsilon)\,. \tag{5.23}$$

Notice that the term $\varepsilon\,\cos k\,y$ has disappeared from equation (5.23) the solution of which is

$$S(t) = S_\infty + [S(0) - S_\infty]\;\mathrm{e}^{-2k^2 D_{\parallel}\,t} \quad \text{with } k = \frac{2\pi}{H}\,. \tag{5.24}$$

By fitting the numerical results of $S(t)$ obtained from (5.6) to the form of equation (5.24), it is possible to extract the coefficient $D_{\parallel}$. Figure 16 shows the numerical values of $S(t)$ evaluated at a volume fraction $\phi = 0.35$, with $N = 27$ particles, as well as the curve fit according to equation (5.24).

Before accepting this curve fit, however, it is necessary to check that these results do not depend on the particular choice of the initial distribution for the configurations used in the calculations. A good parameter characterizing the structure of the suspension at the initial time $t = 0$ is $S(0)$ which equals the static structure factor of the initial particle distribution at the lowest wavenumber (for more details, see Berne & Pecora 1976, p. 225). Different independent initial ensembles were therefore generated having different values of $S(0)$, and $S(t)$ was determined from simulations which were performed starting from these initial ensembles. The results obtained for

https://doi.org/10.1017/S0022112001005122 Published online by Cambridge University Press

N	N_c	$1/H$	$D_\parallel$	$D_\perp$
16	512	0.1735	0.10 ± 0.05	0.08 ± 0.03
27	256	0.1457	0.13 ± 0.05	0.11 ± 0.02
54	128	0.1157	0.15 ± 0.08	0.17 ± 0.02
64	128	0.1093	0.18 ± 0.04	0.18 ± 0.02
∞		0	0.20 ± 0.05	0.21 ± 0.02

TABLE 4. Values of the gradient diffusivities evaluated for a volume fraction of $\phi = 0.35$, with N the number of particles in the unit cubic cell, N_c the number of configurations in the ensemble, and $1/H$ is the inverse of the height of the cell. The values for $1/N = 0$ were obtained by linear extrapolation.

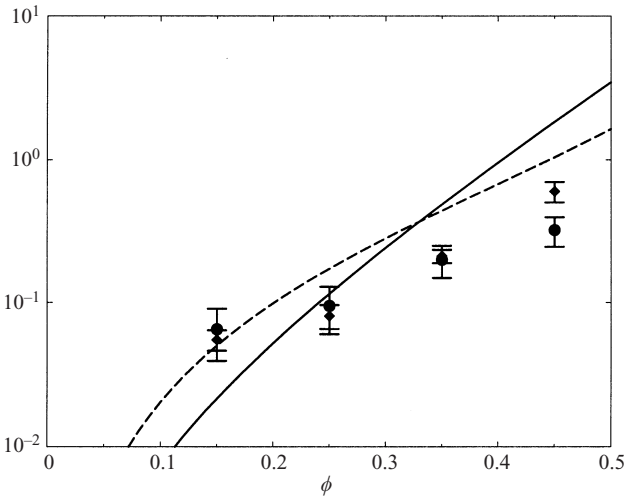


FIGURE 17. Values of $D_\parallel$ (circles) and $D_\perp$ (diamonds) extrapolated to $1/N = 0$ as functions of the volume fraction ϕ. The solid line is D_1 as defined in equation (5.25) and the dashed line is D_2 as defined in equation (5.26).

the gradient diffusivity were found to be in agreement with each other within the measured error, i.e. the error found in fitting $S(t)$ using equation (5.24). As might have been anticipated, ensembles with higher values of $S(0)$ gave smaller errors in $D_\parallel$. For this reason ensembles with high $S(0)$ values, usually between 0.5 and 1.0, were used in subsequent simulations.

The gradient diffusivity in the direction normal to the plane of shear $D_\perp$ can be evaluated, using exactly the same method as for $D_\parallel$, by substituting the spatial coordinate z for y and the velocity component w for v. The results for both $D_\parallel$ and $D_\perp$ are reported in table 4, for a volume fraction $\phi = 0.35$, as obtained with a different number of particles in each unit cell and a different number of configurations. Again, as in the case of the tracer diffusivities, these diffusion coefficients are dependent on the number of particles in the unit cell and therefore, as before, a linear regression in $1/N$ was used to extrapolate the results to the limiting case of an infinitely large cell, which, incidentally, also corresponds to $k \to 0$. In Figure 17 the gradient diffusion coefficients $D_\parallel$ (circles) and $D_\perp$ (diamonds), extrapolated to $1/N = 0$, are plotted as functions of the volume fraction. Note that, as in the experimental results, the values of two coefficients are close to each other.

https://doi.org/10.1017/S0022112001005122 Published online by Cambridge University Press

Since no previous numerical results exist to which our data can be compared, the only possible comparison is with experimental findings, but no method currently exist for measuring the gradient diffusion coefficient directly. By fitting particle migration data to the solution of model equations, however, Leighton & Acrivos (1987*b*) were able to extract values for the gradient diffusivity at constant stress which they then fitted with the expression

$$D_1 = \tfrac{1}{3}\phi^2(1 + \tfrac{1}{2}\mathrm{e}^{8.8\phi}). \tag{5.25}$$

An alternative expression for the gradient diffusivity was given by Phillips *et al.* (1992),

$$D_2 = 0.65\,\phi^2 \frac{1}{\eta}\frac{\mathrm{d}\eta}{\mathrm{d}\phi}\,, \tag{5.26}$$

where η is the effective relative viscosity of the suspension taken to be

$$\eta = \left(1 - \frac{\phi}{0.68}\right)^{-1.82}. \tag{5.27}$$

In figure 17, D_1 given by (5.25), is plotted as a solid line and D_2, as defined by equation (5.26), as a dashed line. Clearly both are in fair agreement with the values for the diffusion coefficient as obtained from our numerical simulations and extrapolated to $1/N = 0$.

As mentioned earlier, our technique for computing the gradient diffusivity has some points in common with the well-known method for determining the tracer as well as the gradient diffusivity from light scattering experiments (Rallison & Hinch 1986). Nevertheless, the two methods differ in at least one important respect. Specifically, in the latter case, the diffusivity is determined via the *dynamic* structure factor which measures the time autocorrelation function of the fluctuations in the particle number density. On the other hand, the function $S(t)$ of (5.6) refers to the evaluation of the instantaneous *static* structure factor which, in turn, is related to the evolution of the instantaneous mean-square fluctuations of the number density as the suspension is being sheared. As a result, $S(t)$ does not vanish as $t \to \infty$, in contrast to the dynamic structure factor, and its asymptotic value S_∞ reflects the statistics of the particle configuration which is attained after the suspension has been sheared for large values of the strain starting from an initial set of hard-sphere configurations.

6. Summary and concluding remarks

The flow of a monodisperse, neutrally buoyant, homogeneous suspension of non-Brownian solid spheres in simple shear was simulated via Stokesian dynamics starting from a large number of independent hard-sphere configurations and ensemble averaging the results. We established that the particle displacements in the directions normal to the flow have Gaussian distributions, the variances of which grow quadratically for small times, hence implying the absence of short-time self-diffusion in contrast to Brownian suspensions, and linearly with time but only for time scales exceeding the correlation time which itself is quite large (shown in table 3). By extending the computations to longer time intervals than had been done previously, we were thereby able to compute the long-time self-diffusivities (shown in figure 10) for a suspension of non-Brownian particles subjected to shear flow. Our procedure, which also permitted us to evaluate the autocorrelation for the velocities in the directions normal to the flow, has the great advantage of breaking up the computational effort of a single long simulation into a number of more affordable short-lived independent simulations and

https://doi.org/10.1017/S0022112001005122 Published online by Cambridge University Press

ϕ	$\hat{D}_{yy}$	$\tilde{D}_{yy}$	$\hat{D}_{zz}$	$\tilde{D}_{zz}$	$D_{\parallel}$	$D_{\perp}$
0.15	0.005 ± 0.002	0.003 ± 0.002	0.002 ± 0.0005	0.002 ± 0.001	0.07 ± 0.03	0.06 ± 0.01
0.25	0.017 ± 0.004	0.015 ± 0.0005	0.006 ± 0.001	0.004 ± 0.001	0.10 ± 0.03	0.08 ± 0.02
0.35	0.041 ± 0.007	0.037 ± 0.012	0.016 ± 0.002	0.017 ± 0.003	0.19 ± 0.05	0.21 ± 0.02
0.45	0.051 ± 0.007	0.056 ± 0.006	0.039 ± 0.005	0.036 ± 0.005	0.32 ± 0.08	0.60 ± 0.10

TABLE 5. Summary of the values of the self- and gradient diffusivities evaluated for different volume fractions, obtained by linear extrapolation to $1/N = 0$.

is especially advantageous in computations using a parallel machine or a cluster of computers. We further confirmed that the integrals of these velocity autocorrelation functions produce an alternative way of determining the self-diffusivities. We also found that, upon reversal of the direction of shear, the particles trace back their trajectory but only for a time that is shorter than the correlation time, after which they continue their diffusive motion as if the flow reversal had never occurred.

Finally, a new method, motivated by the work of Marchioro *et al.* (2000, 2001), was developed for computing the gradient diffusion coefficients directly from numerical simulations. This method is based on artificially alterating the probability of an ensemble of configurations flowing under shear so that, according to the new probability density, defined in equation (5.3), the suspension becomes slightly inhomogeneous and a flux of particles is thereby generated. The balance of the different contributions to the particle flux allows the calculation of the gradient diffusivity. To the best of our knowledge this is the first time that the shear-induced gradient diffusion has been determined directly either experimentally or via numerical computations.

Although all the results referred to above were found to apply even when N, the number of particles within the unit cell, was as low as 16, the numerical values of the diffusion coefficients become significantly larger when N is increased (see tables 2 and 4), in contrast to the effective viscosity which can be computed accurately and independently of N even if the latter is as small as 16 (see e.g. Marchioro *et al.* 2000). Consequently, for each volume fraction ϕ we evaluated these diffusion coefficients for a different number of particles in the unit cell and then extrapolated the results to a cell of infinite extension and therefore containing an infinite number of particles (the results of this extrapolation are shown in table 5 and in figures 10 and 17). But since the errors associated with such extrapolations are, of course, unknown, it would be highly desirable if simulations could be performed with N much larger than 64, the maximum number of particles per unit cell used in this study. This could only be accomplished, however, by employing more powerful computers or more efficient numerical algorithms and techniques than those currently available.

The authors wish to thank Dr J. R. Melrose and Professor J. F. Brady for the use of their simulation codes and for important discussions regarding the oscillations of the intensity of the velocity fluctuations, Professor B. Khusid for his constructive criticisms, Dr Y. Wang for his help during the early stage of this study, and Dr G. Drazer for his numerous and very helpful suggestions.

This work was supported in part by the National Science Foundation under Grant CTS-9711442. This research was also supported in part by the NSF cooperative agreement ACI-9619020 through computing resources provided by the National Partnership for Advanced Computational Infrastructure at the Caltech Center for Advance Computing Research.

https://doi.org/10.1017/S0022112001005122 Published online by Cambridge University Press

REFERENCES

Acrivos, A. 1995 Shear-induced particle diffusion in concentrated suspensions of noncolloidal particles. *J. Rheol.* **39**, 813–826.

Allen, M. P. & Tildesley, D. J. 1987 *Computer Simulations of Liquids*. Oxford University Press.

Ball, R. C. & Melrose, J. R. 1997 A simulation technique for many spheres in quasi-static motion under frame invariant pair drag and brownian forces. *Physica* A **247**, 444–472.

Berne, B. & Pecora, R. 1976 *Dynamic Light Scattering*. Wiley.

Bossis, G. & Brady, J. F. 1987 Self-diffusion of brownian particles in concentrated suspensions under shear. *J. Chem. Phys.* **87**, 5437–5448.

Brady, J. F. 1994 The rheological behaviour of concentrated colloidal dispersions. *J. Chem. Phys.* **99**, 567–581.

Brady, J. F. & Bossis, G. 1985 The rheology of concentrated suspensions of spheres in simple shear flow by numerical simulation. *J. Fluid Mech.* **155**, 105–129.

Brady, J. F. & Bossis, G. 1988 Stokesian dynamics. *Ann. Rev. Fluid Mech.* **20**, 111–140.

Brady, J. F., Phillips, R. J., Lester, J. C. & Bossis, G. 1988 Dynamic simulation of hydrodynamically interacting suspensions. *J. Fluid Mech.* **195**, 257–280.

Breedveld, V., van den Ende, D., Tripathi, A. & Acrivos, A. 1998 The measurement of the shear-induced particle and fluid tracer diffusivities in concentrated suspensions by a novel method. *J. Fluid Mech.* **375**, 297–318.

Breedveld, V., van den Ende, D., Lomgschaap, J. J. J. & Mellena, J. 2000 Shear-induced diffusion and rheology of non-colloidal suspensions: Timescales and particle displacements. *J. Chem. Phys.* **144**, 5923–5936.

Dratler, D. I. & Schowalter, W. R. 1996 Dynamic simulation of suspensions of non-brownian hard spheres. *J. Fluid Mech.* **325**, 53–77.

Folland, G. B. 1984 *Real Analysis*, *Modern Techniques and their Applications*. Wiley.

Foss, D. R. & Brady, J. F. 1999 Self-diffusion in sheared suspensions by dynamic simulations. *J. Fluid Mech.* **401**, 243–274.

Gadala-Maria, F. & Acrivos, A. 1980 Sheared-induced structure in a concentrated suspension of solid spheres. *J. Rheology* **24**, 799–814.

Kreuzer, H. J. 1981 *Nonequilibrium Thermodynamics and its Statistical Foundations*, chap. 11. Clarendon Press.

Leighton, D. & Acrivos, A. 1987*a* Measurement of shear-induced self-diffusion in concentrated suspensions of spheres. *J. Fluid Mech.* **177**, 109–131.

Leighton, D. & Acrivos, A. 1987*b* The shear-induced migration of particles in concentrated suspensions. *J. Fluid Mech.* **181**, 415–439.

Marchioro, M., Tanksley, M. & Prosperetti, A. 2000 Flow of spatially non-uniform suspension. part i: Phenomenology. *Intl J. Multiphase Flow* **26**, 783–831.

Marchioro, M., Tanksley, M. & Prosperetti, A. 2001 Flow of spatially non-uniform suspension. part ii: Systematic derivation of closure relations. *Intl J. Multiphase Flow* **27**, 237–276.

Melrose, J. R. & Ball, R. C. 1995 The pathological behaviour of sheared hard spheres with hydrodynamic interactions. *Europhys. Lett.* **32**, 535–540.

Nott, P. R. & Brady, J. F. 1994 Measurement of shear-induced self-diffusion in concentrated suspensions of spheres. *J. Fluid Mech.* **275**, 157–199.

Phan, S. E. & Leighton, D. T. 1999 Measurement of the shear-induced tracer diffusivity in concentrated suspensions. *J. Fluid Mech.* submitted.

Phillips, R. J., Armstrong, R. C., Brown, R. A., Graham, A. L. & Abbott, J. R. 1992 A constitutive equation for concentrated suspensions that accounts for shear-induced particle migration. *Phys. Fluids* A **4**, 30–40.

Rallison, J. M. & Hinch, E. J. 1986 The effect of particle interactions on dynamic light scattering from a dilute suspension. *J. Fluid Mech.* **167**, 131–168.

Schuster, H. G. 1989 *Deterministic Chaos*, 2nd edn. VCH Verlagsgesellschaft.

https://doi.org/10.1017/S0022112001005122 Published online by Cambridge University Press